Effects of rotor-airframe interaction on the aeromechanics and wake of a quadcopter in forward flight

Denis-Gabriel Caprace[a,b,*], Andrew Ning[a], Philippe Chatelain[b], Grégoire Winckelmans[b]

[a] *Department of Mechanical Engineering, Brigham Young University, Provo, UT 84602, U.S.A.*
[b] *Institute of Mechanics, Materials, and Civil Engineering (iMMC), Université catholique de Louvain, 1348 Louvain-la-Neuve, Belgium.*

Abstract

From small drones to large Urban Air Mobility vehicles, the market of vertical take-off and landing (VTOL) aircraft is currently booming. Modern VTOL designs feature a variety of configurations involving rotors, lifting surfaces and bluff bodies. The resulting aerodynamics are highly impacted by the interactions between those components and their wakes. This has consequences on the aircraft performance and on the downstream wake. Studying the effects of those interactions through CFD can inform the development of cheaper numerical models. In this work, we focus on the interaction between rotors and bluff bodies based on the example of a generic quadcopter in forward flight. Using the Vortex Particle–Mesh method, a CFD method well-suited for wake studies, we analyze the influence of the rotor-airframe interaction on the loads and on the development of the aircraft near wake. Our results show that the presence of the airframe induces a change in average thrust of maximum 2.4% on the rear rotors. Correspondingly, the contribution of the rotors to the overall aircraft lift and drag changes by less than 2%, suggesting that the airframe can be ignored if one seeks a simple model of the rotor forces. On the other hand, the airframe experiences peak loads due to its proximity with the blades. Thus, the

*Corresponding author
Email address: `dcaprace@byu.edu` (Denis-Gabriel Caprace)

rotor-airframe interaction must be accounted for in the prediction of airframe loads. Finally, comparing simulations with and without the airframe, we find that the trailing wake vortices converge to circulations less than 0.2% different. However, the vortex spacing decreases when the airframe is accounted for.
Keywords: aerodynamics, vortex dynamics, vortex particle–mesh method, drone, multirotor, edgewise flight

---

1. Introduction

Today, more and more drones are utilized for various applications including aerial photography, inspection and agriculture. To absorb increasing demand, drones of all sizes are being developed, the smaller ones being not bigger than the palm of the hand. On the other side of the spectrum, the current development of urban air mobility (UAM) pushes for large multirotor vehicles. Often in their operation, the ability to perform vertical take-off and landing (VTOL) is crucial. Modern VTOL aircraft feature varied arrangements of rotors, propellers, lifting surfaces and bluff bodies. One particularly popular design is the quadcopter, such as the drone pictured in Fig. 1 and the UAM vehicle in Fig. 2. Because of their geometry, the aeromechanics of these aircraft are affected by the interactions between the rotors and the airframe, especially when they operate in the wake of one another. At a larger scale, wake interactions may also arise between different aircraft if they cross each other's path. It is therefore crucial to study both the aerodynamic interactions and the wakes to better understand how they affect the aircraft stability and performance (maneuverability, power consumption, etc.). This could help improve the accuracy of simplified aerodynamic models, eventually used to account for wake interactions in the early aircraft design phases. In this work, we use large-eddy simulation to assess the influence of a notional airframe on the aeromechanics of a quadcopter, and on the development of its wake.

Most existing studies address the case of hovering flight. Instead, this work focuses on forward flight. Among recent experimental studies, Yang et al. [2]

Figure 1: A DJI Phantom drone. Credit: DJI technologies, CC BY-SA 3.0, via Wikimedia Commons.

Figure 2: The quadcopter concept UAM vehicle by NASA [1].

measured forces and noise levels of a whole quadcopter in forward flight. Focusing on rotors and their interactions, Stokkermans et al. [4, 3] performed detailed measurements of rotor forces at various incidences, also including the influence of rotor-rotor interactions. CFD has been used to better characterize the aerodynamic interactions between rotors in edgewise flight. Hwang et al. [5], Misiorowski et al. [6] and Pinti et al. [7] qualified the effect of the rotor-rotor interactions on the aircraft forces and moments. Ventura Diaz and Yoon [8] investigated the aerodynamics of quadrotor drones and then later extended their analysis to a large UAM vehicle in [9]. These studies further emphasized the influence of the fine vortical structures generated by the rotors on the rest of the aircraft aerodynamics. From the modeling perspective, adjustments to standard blade element momentum theory were proposed by van Arnhem et al. [10] to predict forces and moments on a rotor subject to arbitrary flow angles, including those typical of forward flight. A range of methods was also proposed to capture rotor-rotor interactions, for example based on momentum theory [11], or an advanced potential flow method [12]. Focusing on wakes, Wang et al. [13, 14, 15] presented results of the CFD of quadcopter wakes. The authors simulated the encounter of a quadcopter wake by another drone to estimate the related hazard. They also examined the effect of the airframe on the near wake topology. However, their modeling of rotors is based on a steady vorticity generation mechanism which results in simplified wakes. Nathanael et al. [16] and Caprace and Ning [17] studied the development and the decay of the far wake of quadcopters, although their simulations neglected the influence of the airframe.

The objective of this work is to determine the effect of the quadcopter airframe on the unsteady loads experienced by each component of the aircraft and the consequence this has on the development of its wake. By comparing two simulations, we aim to highlight the differences in the mechanisms driving the aeroloads and the wake characteristics. We study a drone geometry inspired by the DJI Phantom series, but we postulate that our conclusions also apply to UAM vehicles of similar geometries. Even though the aerodynamics of the drone may differ from larger vehicle's in terms of Reynolds numbers, their wake should not differ significantly as molecular viscosity plays little to no role in the early wake development. Instead, it is dominated by complex vortex dynamics that are scale-independent.

This paper is organized as follows. First, we briefly review the numerical method and models used in this work in Section 2. We give an overview of the Vortex Particle–Mesh (VPM) method, and its extension to model rotor blades and bluff bodies such as the drone airframe. To demonstrate the consistency of these models, in Section 3, we present a comparison of their numerical predictions to experimental measurements on an isolated propeller at various inflow angles, and on the flow past a circular disk. Subsequently, we present the generic quadcopter model studied in this work in Section 4. Its geometry is inspired by the DJI drone shown in Fig. 1, although greatly simplified. Next, we discuss our simulation results of the quadcopter model in forward flight in Section 5. We determine the influence of the drone airframe by comparing a simulation of the complete drone versus another simulation with only the rotors. We analyse the unsteady and time-averaged loads evaluated on the various drone components in both cases. A similar comparison allows us to identify similarities and differences in the properties of the near wake of the drone. We close the paper with our conclusions as to the effect of the rotor-airframe interaction on the advancing quadcopter.

2. Method

There has been a recent revival of interest in using vortex methods to simulate the aeromechanics of complex vehicles [18, 19]. This work relies on a numerical framework for the large-eddy simulation (LES) of advection-dominated flows that was previously used for the simulation of wind turbine and helicopter wakes [20, 21, 22, 23]. The main component is a flow solver based on the Vortex Particle-Mesh (VPM) method, a hybrid Lagrangian-Eulerian method that has proven robust and efficient for wake computations. The next sections provide a general introduction to the various ingredients in this numerical framework, and more details on the modeling of bluff bodies that was recently introduced.

2.1. Flow solver

We solve the incompressible Navier-Stokes equations in their vorticity–velocity formulation:

$$\frac{D\boldsymbol{\omega}}{Dt} = (\nabla\mathbf{u})\cdot\boldsymbol{\omega} + \nu\nabla^2\boldsymbol{\omega} + \nabla\cdot\mathbf{T}^M \,, \tag{1}$$

where $\frac{D}{Dt}$ denotes the Lagrangian derivative, ν is the kinematic viscosity, and $\mathbf{T}^M$ refers to the contribution of the sub-grid scale (SGS) model. The velocity

$\mathbf{u}$ is obtained by solving the Poisson equation

$$\nabla^2 \mathbf{u}_\omega = -\nabla \times \boldsymbol{\omega} \ , \tag{2}$$

and $\mathbf{u} = \mathbf{U}_\infty + \mathbf{u}_\omega$ where $\mathbf{U}_\infty$ is the free stream velocity.

To advance these equations in time from an initial condition, the VPM method takes advantage of the combination of two disctretizations: a set of Lagrangian particles, and an underlying cartesian grid with a mesh size h. Each particle is characterized by its position $\mathbf{x}_p$, volume $V_p = h^3$ and strength $\boldsymbol{\alpha}_p = \int_{V_p} \boldsymbol{\omega} \, d\mathbf{x} = \boldsymbol{\omega}_p \, V_p$. Initially, there are as many particles as grid cells, and the particles are aligned with the grid. As the particle move over time, high order interpolation schemes are employed to pass information back and forth between the particles and the mesh.

The time integration employs a third order Runge-Kutta scheme. Over the course of a time step, the solution of Eq. (2) is first computed on the grid, and the velocity field is then interpolated onto the particles. This provides the massive advantage for the Poisson solver to operate in Fourier space, benefiting from an efficient 3-D fast Fourier transform algorithm originally presented in Chatelain and Koumoutsakos [24]. Then, the position and strength of the particles are updated in a Lagrangian fashion, by solving Eq. (1) recast into

$$\frac{d\mathbf{x}_p}{dt} = \mathbf{u}(\mathbf{x}_p) \, , \tag{3}$$

$$\frac{d\boldsymbol{\alpha}_p}{dt} = \left((\nabla \mathbf{u}) \cdot \boldsymbol{\omega} + \nu \nabla^2 \boldsymbol{\omega} + \nabla \cdot \mathbf{T}^M \right)_p \, V_p \, . \tag{4}$$

Taking advantage of the grid again, the right-hand-side of Eq. (4) is also first evaluated using finite differences. As noted in previous works, the constraint on the time step associated with this hybrid formulation is less stringent than in ordinary Eulerian solvers, which constitutes another advantage of the method. To summarize, the Lagrangian treatment of the advection yields a numerical method with low dissipation and dispersions errors, while the use of the Eulerian grid for costly operations enables high computational performance.

Two additional operations are necessary to guarantee the accuracy of the simulations. *Remeshing* consist in periodically replacing the entire set of particles by a fresh one aligned with the grid; this prevents particles from depleting some regions of the flow or clustering in others when time advances. The *reprojection* operation, on the other hand, helps maintain the solenoidal property of the vorticity field, which is otherwise not directly enforced by the solver.

We refer the reader to the reviews by Winckelmans [25], by Mimeau and Mortazavi [26], and references therein for further details on the VPM method and on its theoretical grounds. Additionally, Chatelain et al. [27] provide a thorough description of the present implementation on massively parallel architectures, based on the open-source PPM library [28].

2.2. Blade model

The rotor blades are accounted for through the Immersed Lifting Line (ILL) method presented in [29], and implemented as in [23]. Similarly to many lifting or actuator line techniques, the ILL replaces each blade with its quarter chord line. The line is discretized in the spanwise direction with elements of a size close to h (the mesh size of the VPM grid). Based on the instantaneous velocity and angle of attack evaluated at the center of each blade segment, the local sectional lift and drag are retrieved from tabulated airfoil polars. Then, under the assumption of quasi-unsteady flow around the airfoil, the circulation $\mathbf{\Gamma}$ around the local 2-D airfoil is recovered from the Kutta-Joukowski theorem,

$$\boldsymbol{\ell} = \frac{1}{2}\rho\,|\mathbf{U}_{\mathrm{rel}}|^2 c\, C_\ell\, \hat{\mathbf{e}}_\ell = \rho\,\mathbf{U}_{\mathrm{rel}} \times \mathbf{\Gamma}\ , \tag{5}$$

where $\boldsymbol{\ell}$ is the sectional lift per unit span on the segment, $\mathbf{\Gamma}$ is the circulation vector (along the spanwise direction), c is the local airfoil chord, and C_ℓ is the lift coefficient retrieved from airfoil polars. The relative blade-air velocity $\mathbf{U}_{\mathrm{rel}} = \mathbf{U}_\infty + \mathbf{u}_\omega - \mathbf{U}_{kin}$ accounts for the free stream velocity, the velocity induced by all the vorticity present in the simulation, and the kinematic velocity of the line, repsectively. A similar treatment is employed to compute the sectional drag.

The subsequent numerical treatment by the ILL method is fully compatible with a Lagrangian discretization, as illustrated in Fig. 3. The blade segments are

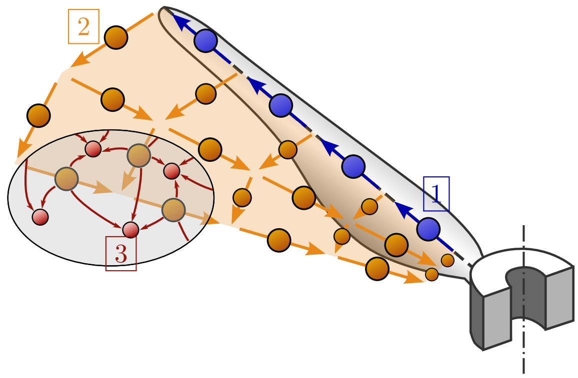

Figure 3: Immersed lifting line technique with $\boxed{1}$: computation of the bound vortex particles (in blue), $\boxed{2}$: shedding of the wake particles (in orange), $\boxed{3}$: merging of shed particles with bulk flow particles (in red).

represented with a set of equivalent bound vorticity particles of circulation $\mathbf{\Gamma}$, calculated from Eq. (5). New particles are shed from the line over the course of a time step. Their circulation is obtained as the spanwise variation of the bound circulation for the streamwise-oriented particles, and as the time variation of the bound circulation for the particles parallel to the line. All shed particles are subsequently merged with the pre-existing flow particles so that the total number of particles in the simulation remains constant. Again, we refer the reader to the above publications for the implementation details.

2.3. Airframe and body model

Solid bluff bodies such as an airframe are incorporated in the simulation environment using a penalization of the Navier-Stokes equations *à la* Brinkman [30]. Our objective in employing this technique is to capture the influence of the airframe on the aerodynamics of the rotor and their wakes. It is not intended to capture the details of the boundary layers developing at the surface of the body, as this would result in prohibitively expensive simulations. Instead, the penalization is used as a convenient model to account for the presence of the airframe (as was done in previous studies such as in [31]).

The penalization method adds a term to the momentum equations in order to force the local velocity of the fluid $\mathbf{u}$ to match the velocity of the body $\mathbf{u}_b$ inside the body. For instance, the last term of

$$\frac{D\mathbf{u}}{Dt} = \frac{\nabla p}{\rho} + \nu\nabla^2\mathbf{u} + \lambda\chi\left(\mathbf{u}_b - \mathbf{u}\right) \tag{6}$$

is the penalization term. λ is a parameter that has units of s^{-1} and controls how effective the penalization is. The higher λ, the closer to zero $\mathbf{u}_b - \mathbf{u}$ inside the body [32]. The location of the body itself is parametrized using the mask function χ equal to 1 inside the body and 0 outside. To mitigate the numerical noise due to the non-coincident intersection between the body boundary and the mesh, a smoothing function is introduced that handles the transition from $\chi = 0$ to $\chi = 1$ continuously, over a distance approximately equivalent to one computational cell. Figure 4 illustrates the mask, the underlying cartesian grid, and the smoothing function used in this work, where ζ is a local coordinate normal to the boundary.

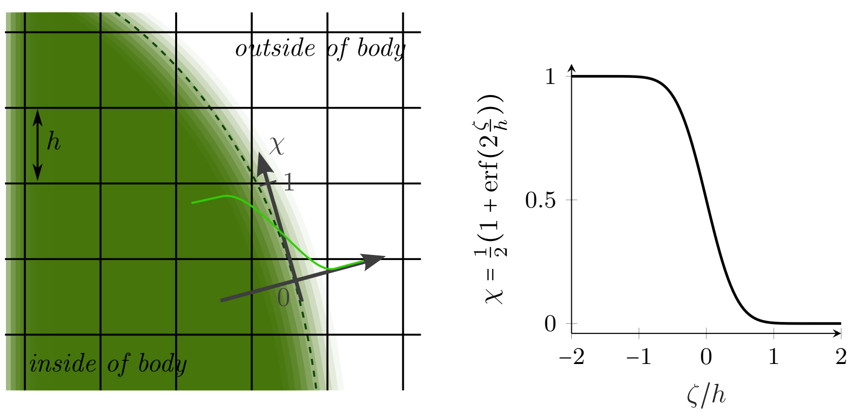

Figure 4: Penalization mask function χ in a 2D example.

Our implementation of the penalization is inspired by the semi-implicit numerical scheme proposed by Rasmussen et al. [33] in vorticity-velocity formulation. Considering a splitting of the operators over the course of a time step between the penalization and the rest of the Navier-Stokes solver, we first compute an updated $\mathbf{u}^*$ that corrects the velocity for the presence of the body at the beginning of every computational step. The implicit —hence unconditionally stable— penalization operator reads

$$\frac{\mathbf{u}^* - \mathbf{u}^n}{\Delta t} = \lambda\,\chi\,(\mathbf{u}_b - \mathbf{u}^*), \tag{7}$$

and the correction on the velocity field is thus obtained as

$$\Delta\mathbf{u} = \mathbf{u}^* - \mathbf{u}^n = \frac{\lambda\,\Delta t\,\chi}{1 + \lambda\,\Delta t\,\chi}(\mathbf{u}_b - \mathbf{u}^n). \tag{8}$$

To make the penalization effective, the product $\lambda\,\Delta t$ has to be large (e.g., $\lambda\,\Delta t > 10^3$) [34]. Thus, as suggested in [33], an even simpler implementation consists in replacing the flow velocity with the prescribed velocity inside the body,

$$\Delta\mathbf{u} = \mathbf{u}^* - \mathbf{u}^n = \chi\,(\mathbf{u}_b - \mathbf{u}^n). \tag{9}$$

We used the latter for this work. In what follows, we also always have $\mathbf{u}_b = \mathbf{0}$.

Since we directly work with the vorticity field, we compute the corresponding correction obtained as

$$\boldsymbol{\omega}^* = \boldsymbol{\omega}^n + \nabla \times (\Delta\mathbf{u}). \tag{10}$$

The corrections (9) and (10) are applied to the grid velocity and vorticity fields, respectively. It is done prior to computing the other terms in the right-hand side of Eq. (4). The rest of the VPM algorithm then operates as usual.

Note that more accurate results can be obtained with penalization techniques as in [35, 36], at the cost of introducing sub-iterations between the penalized vorticity and velocity fields, which increases the computational costs. As we are merely interested in a model of the airframe, we used the simple non-iterated implementation here.

2.4. Evaluation of aerodynamics forces

One of the valuable outputs of the present numerical framework is the instantaneous evolution of the forces and moments exerted on each model component. During a simulation, we evaluate separately the forces and moments on each blade segment, and on the solid body; these diagnostics are used to emphasize the aerodynamic interactions characterizing the selected operating conditions.

As far as the blades are concerned, the instantaneous sectional lift and drag coefficients are internal states of the lifting line model presented above. The corresponding force developed at each blade section is determined based on these coefficients and the local relative flow velocity. The overall rotor forces and moments are recovered by summing the contribution of each blade element.

For the solid body, the aerodynamic forces and moments are derived from the momentum correction that the penalization introduces in the Navier-Stokes equations [34, 37]. In practice, we approximate the change of momentum imparted by the penalization with

$$\frac{\mathbf{F}}{\rho} = -\frac{1}{\Delta t}\int_{\Omega} \Delta\mathbf{u}\, dV, \tag{11}$$

and the corresponding moment with

$$\frac{\mathbf{M}}{\rho} = -\frac{1}{\Delta t}\int_{\Omega} (\mathbf{x} \times \Delta\mathbf{u})\, dV, \tag{12}$$

where Ω is the computational domain. These integrals are evaluated numerically on the grid at every time step using a mid-point quadrature.

3. Assessment of the model predictions

3.1. Blade model

A previous investigation compared the thrust and torque predicted by the ILL method to experimental results on hovering helicopter rotors [23]. The thrust predictions were found to agree very well with experimental data, while the torque was within 10 to 15% of the expected value in the worst case. The sensitivity of the predicted loads to the airfoil polars used in the model was also highlighted. This section presents further comparisons to show how the blade model performs in the case of a propeller at a variety of inflow angles.

We simulate the *TU Delft F29* propeller and we compare the rotor forces and moments predicted numerically to the experimental measurements reported by Stokkermans et al. [3]. This four-bladed propeller has a diameter $D = 0.3048\ m$. In the experimental setup, the propeller blades are mounted on a hub, on top

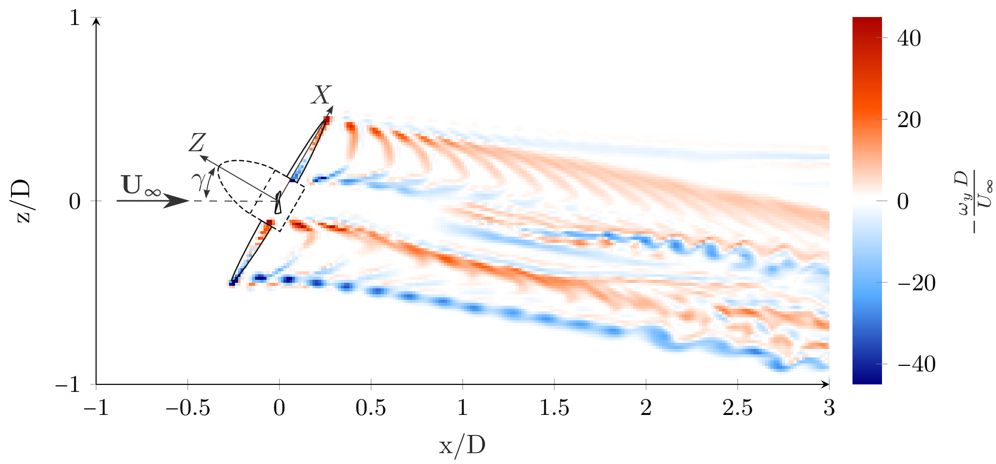

Figure 5: Snapshot of the vorticity shed by the F29 propeller at $\gamma = 30°$, with the propeller geometry overlaid.

of which a spinner is attached. On the other end, this rotating ensemble is connected to a fixed cylindrical nacelle that has the same diameter as the hub. We limit our study to the case of the isolated rotor at an advance ratio of $J = \frac{U_\infty}{nD} = 0.49$, where n is the revolution frequency and U_∞ is the norm of the inflow velocity. This advance ratio is similar to that of the quadcopter rotors we study later in this work. In this first assessment of the ILL method on the F29 propeller, only the blades are modeled in the simulations; the hub, spinner and nacelle are not accounted for. The configuration is depicted in Fig. 5 which also shows a snapshot of the computed vorticity field in a cross section that goes through the center of the rotor. The hub and the spinner are shown for reference in the figure.

The blades are modeled as straight lifting lines, and their chord and twist are based on the distributions shown in Fig. 6. The actual interpolated distributions utilized in the simulations is available in the supplemental data repository [38]. As was done in [23], the chord distribution is slightly adjusted in the tip and root regions to ensure that the loading goes to zero at each blade end. The blade geometry is based on 17 distinct airfoil sections distributed along the radius. Each segment of the lifting line is assigned to a given airfoil following the distribution shown in the figure. For each airfoil, the aerodynamic polar is obtained as follows: the sectional force and moment coefficients are first computed using XFOIL [39] at the average Reynolds number expected for the corresponding radial location, a Mach number of 0.0, and an arbitrary $N_{\text{crit}} = 5$. This relatively low N_{crit} was chosen to reflect the operation of the blade in a turbulent environment (expected when γ increases). The XFOIL outputs are then filtered to remove numerical oscillations, and extended using Viterna and Janetzke [40] method, resulting in a smooth polar defined over 360 degrees. The complete set of polars used in our computations is provided in the supplemental data repository [38]. Compressibility effects are accounted for directly during the simulations by applying the Prandtl-Glauert correction based on the locally probed $\mathbf{U}_{\text{rel}}$ and assuming a speed of sound of 340 m/s.

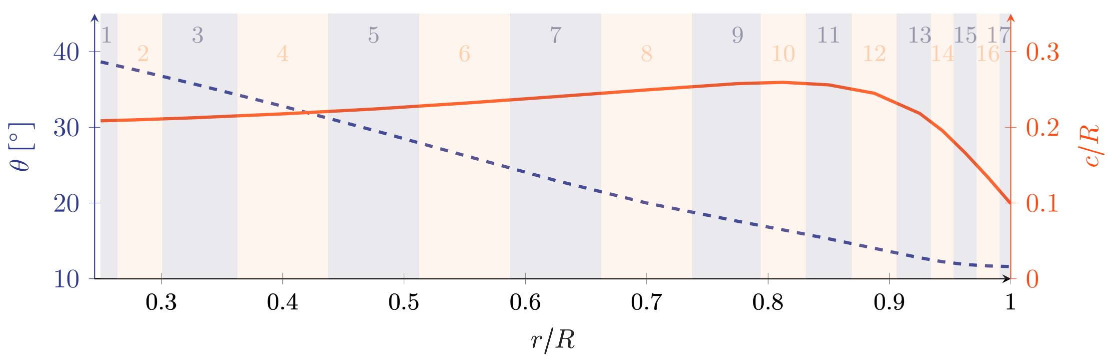

Figure 6: Twist (- - -) and chord (——) distributions of the F29 propeller documented in [3]. The number in the shaded areas correspond to the airfoil section index.

We simulated three different spatial resolutions: 32, 48 and 64 particles per rotor diameter. Recall that, due to the hybrid character of the VPM, the number of particles is equivalent to a number of grid cells, with h the mesh size. From the computational perspective, the finest simulations costed about 160 CPUh per one rotor revolution and maintained approximately 14 million particles.

The rotor forces and moments predicted from our simulations are compared to the experimental measurements in Fig. 7. The total rotor forces and moments are computed as the sum of the contributions from each airfoil section (lift, drag and pitching moment) on every blade. We report the thrust coefficient C_T, and the edgewise force coefficients C_X, C_Y. We also examine the power coefficient C_P, the rolling moment coefficient C_l, and the pitching moment coefficient C_m —all calculated about the rotor center. These quantities are defined as

$$\begin{aligned} C_T &= \frac{F_Z}{\rho n^2 D^4}, \quad C_X = \frac{F_X}{\rho n^2 D^4}, \quad C_Y = \frac{F_Y}{\rho n^2 D^4}, \\ C_P &= \frac{2\pi M_Z}{\rho n^2 D^5}, \quad C_l = \frac{M_X}{\rho n^2 D^5}, \quad C_m = \frac{M_Y}{\rho n^2 D^5}, \end{aligned} \tag{13}$$

where the subscript of the forces F and moments M indicates the component in the rotor frame (shown in Fig. 5). The coefficients are time-averaged over two rotor revolutions after the initial transient.

First, for most of the coefficients, we observe that the values only marginally change when the spatial resolution increases. The effect is more pronounced on the thrust coefficient, and it can be seen that C_T converges when h/D decreases.

The agreement between experimental data and numerical predictions is generally fair, even though some discrepancies stand out. The most obvious mismatch concerns C_X for $\gamma > 0$. It is explained by the fact that the experimental measurements include the contributions from the blades, the hub and the spinner, while the numerical setup only considers the blades. As a result, our predictions underestimate the C_X measurements, mostly because of the absence of the hub and spinner drag. For the same reason, the pitching moment C_m is also underestimated, although to a lesser extent. In the experiment, the spinner further affects the aerodynamics of the blades when they pass in its wake, which may contribute to the small discrepancy observed on C_T and C_Y at $\gamma = 60°$ and part of the discrepancy at 90°. For the latter angle, another phenomenon causes larger differences. An inspection of the flow field revealed that, at $\gamma = 90°$, the tip vortex shed on the fore part of the disk initially travels above the rotor prior to being advected downwards. As a result of this trajectory, the succeeding blade passes exactly through the middle of the preceding tip vortex. A similar blade-vortex interaction (BVI) was previously identified as the main cause for inaccurate tip loads due to the limitations of the lifting line approach [23]. We

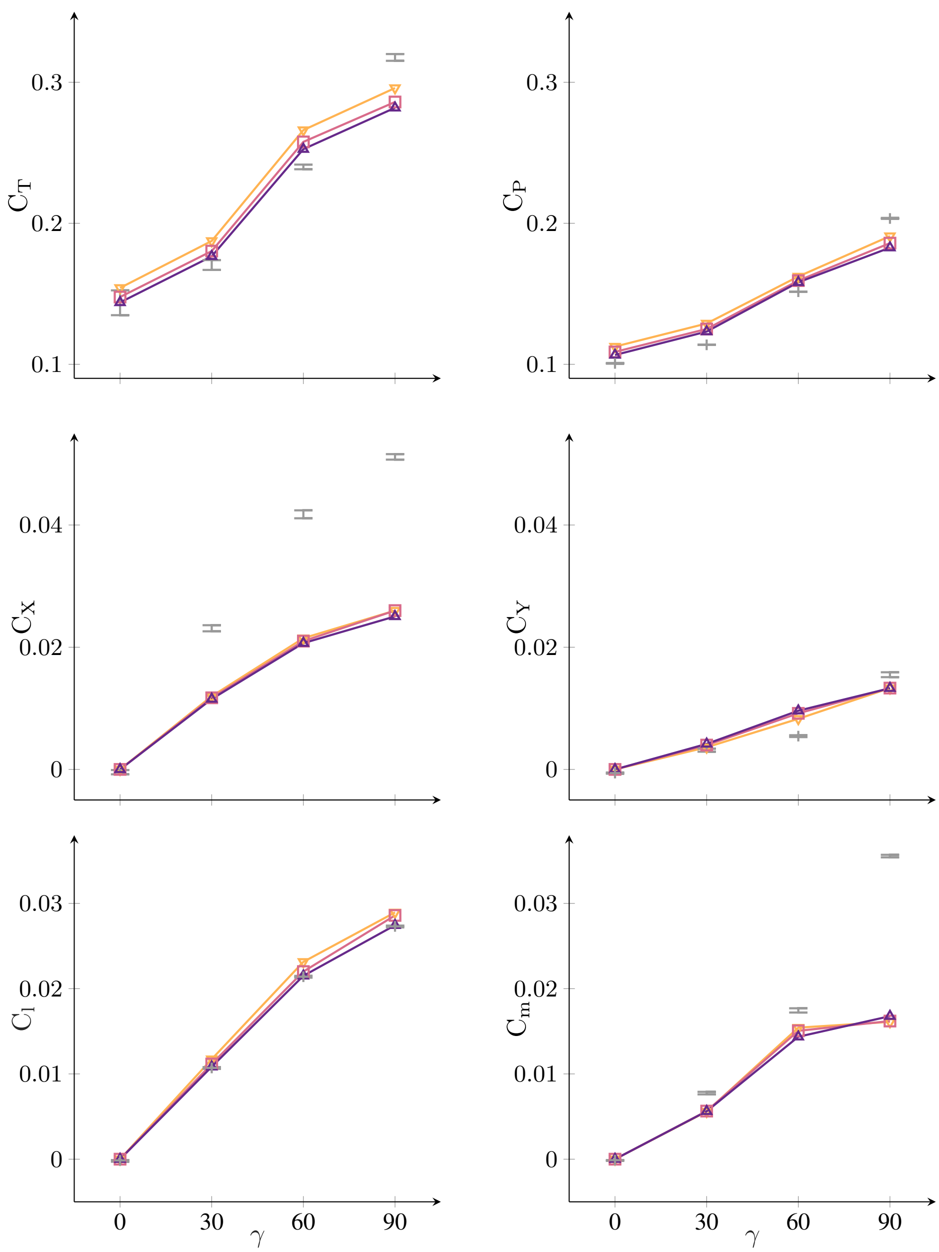

Figure 7: Time-averaged rotor coefficients evaluated at a resolution of $h/D = 1/32$ ( ), 1/48 ( ) and 1/64 ( ), compared to the range of measured average value [3] ( ).

believe the same mechanism is here at play, leading to underpredicted tip loads in the fore part of the disk, and hence affecting all the rotor coefficients with a mostly apparent signature on C_m and C_T. For the rest, the power coefficient remains within 10% of the expected value at all angles, which is consistent with the observation made in the hover case [23]. Generally speaking, we should also mention that lifting line-based models are known to suffer from inaccurate tip load predictions. Such a behavior is common to various types of actuator line techniques [41].

The comparison just shown and the related discussion may serve as a reference to assess the level of accuracy that can be expected from the ILL method. Even though this model has some limitations, it captures the relevant trends on the loads, except perhaps when a blade comes in direct contact with a tip vortex. Additionally, a feature of the model that the above comparison does not reflect is the proper shedding and advection of vorticity throughout the computational domain. This is crucial for capturing the vortex interactions and the ensuing wake development, which is one of the focuses of this study.

3.2. Airframe and body model

The validity of the newly implemented airframe model is assessed based on the flow past a circular disk of diameter D at high Reynolds numbers. This case has been studied experimentally by Roos and Willmarth [42] and by Berger et al. [43]. They showed that the drag experimented by the disk is almost insensitive to the Reynolds number when $Re_D = \frac{U_\infty D}{\nu} > 10^3$. Results of numerical simulation were also presented by Tian et al. [44]. The authors used a conventional grid-based CFD solver to simulate the flow at $Re_D = 1.5 \cdot 10^5$.

The geometry of our numerical setup is depicted in Fig. 8, together with a visualization of the time-averaged flow from one of our simulations. We simulated the configuration at $Re_D = 10^4$ with three different spatial resolutions. Table 1 compares the predicted drag coefficient and recirculation length to experimental and numerical reference values. The drag coefficient is defined as $\overline{C_D} = \frac{\bar{F}_x}{1/8\,\rho U_\infty^2\,\pi D^2}$, where $\bar{F}_x$ is the time-averaged streamwise force evaluated

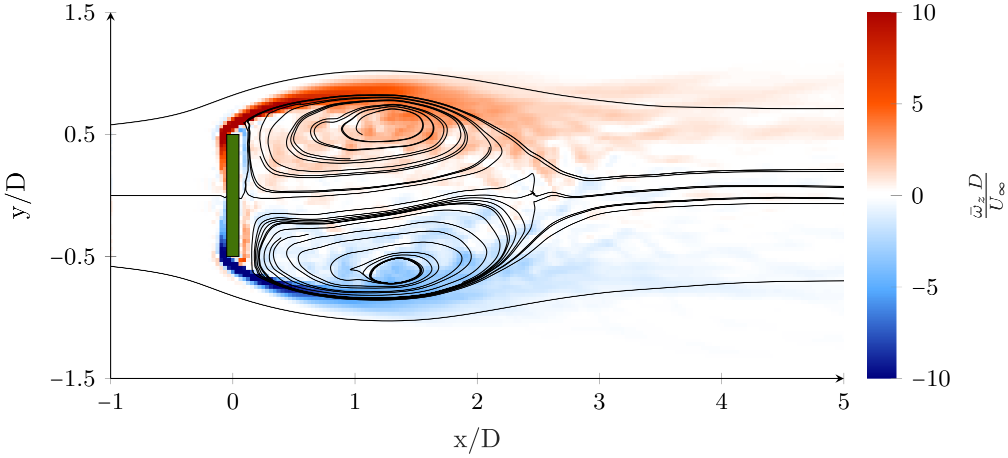

Figure 8: Time-averaged vorticity computed for the case $h/D = 1/32$, and streamlines of the averaged flow.

following the method presented in Section 2.4. The recirculation length, $\overline{L_w}$, is the streamwise location of the stagnation point in the time-averaged flow which marks the end of the recirculation region. It is here determined from visual inspection. All time averages are performed over 15 seconds of physical time after the initial transient.

Case	$\overline{C_D}$	$\overline{L_w}/D$
$h/D = 1/16$	1.497	2.84
$h/D = 1/24$	1.335	2.79
$h/D = 1/32$	1.272	2.46
Exp. [42]	1.15 – 1.28	–
Exp. [43]	–	2.5
CFD [44]	1.124 – 1.135	2.29 – 2.64

Table 1: Comparison of the time-averaged drag coefficient and recirculation length of the circular disk.

The predictions from the present simulations are in fair agreement with the experimental data, both in terms of drag (load prediction) and recirculation length (flow prediction). The coarse resolution tends to overestimate both metrics, but the values converge to well within the range of the experimental values when h/D decreases. The grid-based CFD converges to a slightly smaller $\overline{C_D}$ and $\overline{L_w}$, although the authors of [44] deem the agreement acceptable. Additionally, the average flow field shows very similar recirculation patterns as those presented in [44], which further attests to the consistency of our model.

Overall, this demonstrates the proper implementation of the pemalization method in our code. It also shows that the airframe model captures the flow blockage as intended.

4. Quadcopter model

We study a quadcopter model inspired from the Phantom drones manufactured by DJI. Because the actual geometry is not publicly available, we propose a simplified and easily reproductible geometry that mimics the original drones. It includes the blades of the four rotors and the drone airframe, but without the camera and the landing skids. The resulting geometry is shown in Fig. 9. In the rest of this work, we refer to it as *generic DJI*.

The drone airframe consists of a notional shape made of four conical legs. The union of the legs defines the mask function that is used in the penalization technique. The electric motors and rotor hubs that are visible on the original drone (Fig. 1) are not modeled. The dimensions of the airframe and rotor blades are specified in Fig. 9. Mind the definition of the X, Y, Z frame in the figure.

All rotors are 2-bladed and lie in the same plane that is parallel to the plane formed by the two major axes of the airframe, represented by dark dash-dotted lines. Their intersection marks the center of the airframe. As classically done for quadcopters, the direction of rotation of rotors 1 and 3 is opposite to that of rotors 2 and 4; this is to ensure controllability. When the aircraft is in forward flight, the nominal orientation is such that the upstream velocity comes from the left using the representation of the figure. Therefore, rotors 1 and 2 are hereafter referred to as front rotors, and 3 and 4 as rear rotors. In this configuration, the

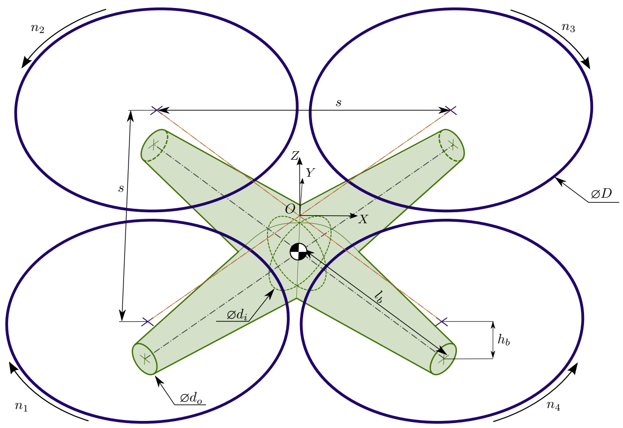

$$
\begin{aligned}
D &= 0.2400\ m\\
s &= 0.2500\ m\\
h_b &= 0.0450\ m\\
l_b &= 0.1800\ m\\
d_i &= 0.0700\ m\\
d_o &= 0.0385\ m
\end{aligned}
$$

Figure 9: The generic DJI model used in this study. The rotors (represented with circles) are labeled from 1 to 4 as shown. The blades are not shown.

blades of the front rotors are advancing on the outboard side, while the blades of the rear rotors are retreating outboard. Also, rotors 1 and 4 belong to the left (or port) side, whereas 2 and 3 are on the right (or starboard) side.

Similarly to the propeller studied in Section 3.1, the blades are modeled as straight lifting lines. Considering that data on the original blades of the DJI Phantom 3 are not directly provided by the manufacturer, we choose to work with the blade design proposed by Ning [45] that is better documented [46, 18]. Figure 10 shows the chord and twist distributions that we base our blade model on. Again, the actual interpolated distributions used in the simulations is available in the supplemental data repository [38]. Note that the blades have a fixed pitch (i.e., there is no collective pitch control).

The blades are outfitted with two distinct airfoils along the radius R: the *E856* profile from the blade root to $r/R = 0.3$, and the *E63* profile on the outer portion. The polars of each airfoil used in our computations are shown in Fig. 11. Again, these data were computed following the procedure outlined in Section 3.1. However, both polars were here obtained at the same Reynolds number Re_c. This choice was motivated by the fact that the expected average

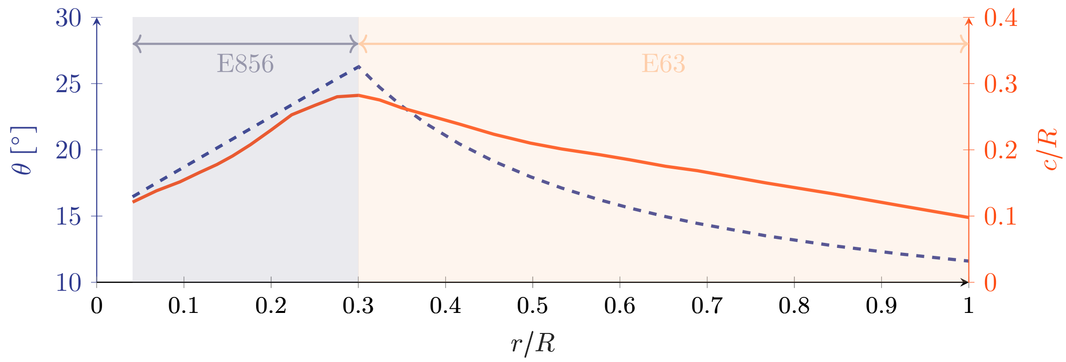

Figure 10: Twist (- - -) and chord (—) distributions obtained from the digitalization of data in [45].

Re_c is fairly constant over the blade. Additionally, compressibility effects were here neglected since the blade tip Mach number is not expected to exceed 0.2.

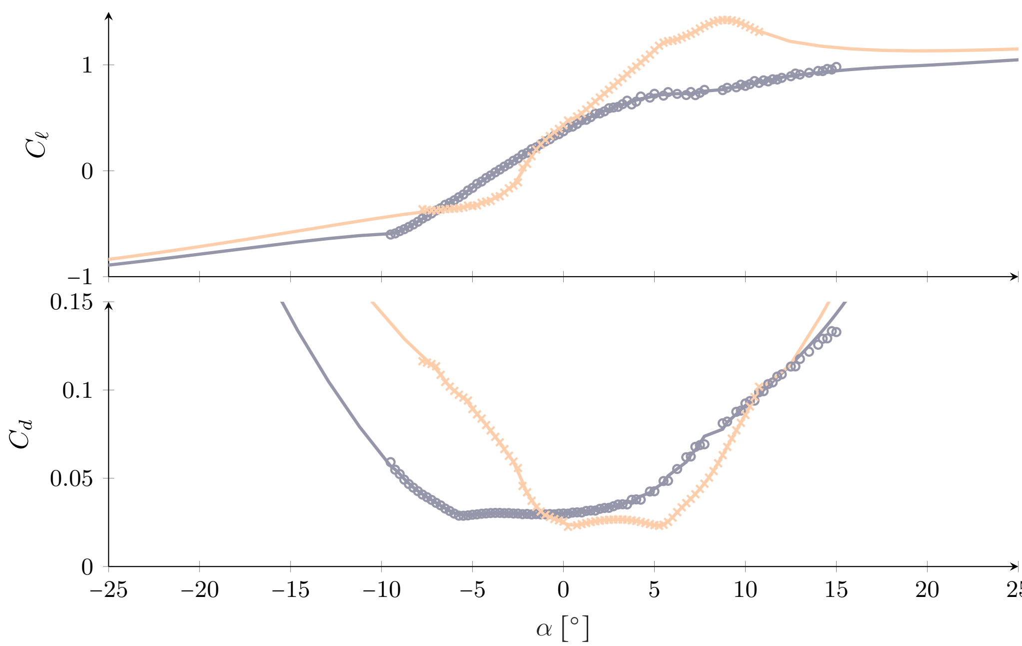

Figure 11: Sectional lift and drag coefficients, as a function of the angle of attack of the E856 ( ) and the E63 ( ) airfoils at $Re_c = 5 \cdot 10^4$. Symbols show the raw XFOIL results, and lines the filtered results.

5. Results

We analyze and compare two simulations in order to determine the influence of the presence of the airframe: the entire drone is considered in the first simulation, whereas only the rotors are simulated in the second one. Both simulations use the same set of parameters summarized in Table 2, where U_∞ is the flight velocity, $n_{\text{front}}, n_{\text{rear}}$ are the revolution frequency of the front and rear rotors, and θ_v is the aircraft pitch angle (positive nose up). Figure 12 shows a 3D visualization of the wake simulated in the *"with airframe"* case.

Table 2: Main operating parameters of the quadcopter in the simulations

U_∞	n_{front}	n_{rear}	θ_v	h/D
$10.00\, m/s$	4250 RPM	5000 RPM	$-13°$	64

In both cases, the same spatial resolution of 64 particles per rotor diameter is utilized. Based on the assessment of the loads presented in Section 3 and on the guidelines that we established from our past experience with the solver [29, 23], this choice represents a good trade-off between accuracy and computational intensity. The computational domain starts $2.25D$ upstream of the center of the drone, while the outflow plane is located $8.25D$ downstream. The boundaries are treated as in [22], including the inflow condition, the outflow condition, and the unbounded lateral boundaries.

Typically, one simulation of the generic DJI geometry is run for approximately 72 hours using 420 CPUs, until a physical time of approximately 0.40 seconds is reached. This corresponds to 1.6 T_c, where $T_c = \frac{L}{U_\infty}$ is the convective time based on the length of the computational domain ($L = 10.5D$). In other words, the computational cost was of approximately 900 CPUh per one revolution of the rear rotors. On average, the simulations maintained approximately 40 million particles.

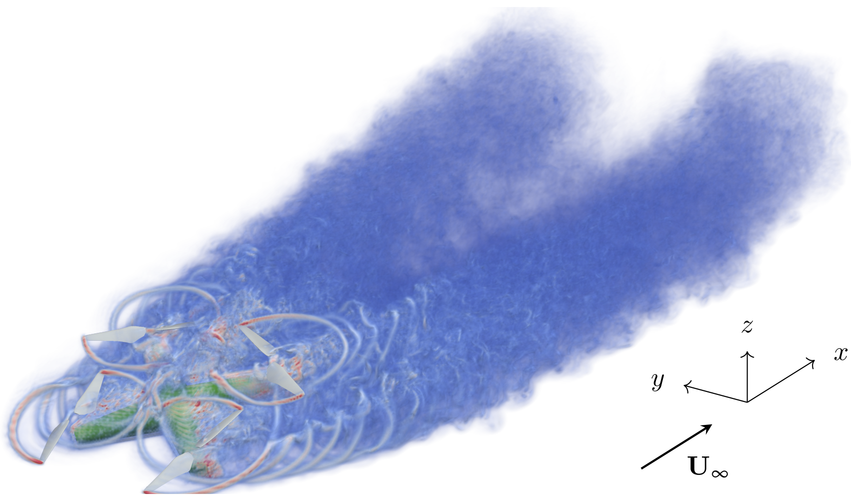

Figure 12: Vizualization of the generic DJI model (*"with airframe"*) and its wake by volume rendering of the vorticity magnitude. This snapshot was taken at $t/T_c = 1.55$. Multimedia view: see attached video.

5.1. Total forces and moments, and trim

The aerodynamic forces and moments on each part of the drone are recovered using the method presented in Section 2.4. In this section, we first verify that the choice of the operating parameters presented in Table 2 yields trim conditions for the *"with airframe"* case. In addition to guaranteeing steady level flight, finding the appropriate trim parameters is also crucial to obtain a realistic wake, since the aircraft operating conditions affect the wake roll-up process and thence the wake properties.

As for many small drones with fixed-pitch propellers, a zero resulting-moment in forward flight is obtained by applying different rotation speeds to the front and rear rotors. The aircraft required lift is obtained by collectively adjusting the rotor speeds, while the thrust is matched by varying the aircraft pitch angle, θ_v. The number of parameters to consider for trim thus reduces to three as we assume the side force and the rolling and yawing moments are zero on average, by symmetry. Generally, computing the trim conditions of a multi-rotor aircraft is difficult due to the unsteady nature of the flow field. The various aerodynamic interactions between the different components of the aircraft further add non-linearity to the problem. In the present case, we determined empirically the appropriate combination of parameters based on trial and error.

The instantaneous forces and moments measured in the simulation of the *"with airframe"* case are presented in Fig. 13. The contributions of the airframe and of all rotor blades together are reported separately. The sum of these two contributions constitutes the total aerodynamic force developed on the model. The time-average of that quantity is also shown. Forces and moments are reported in terms of the non-dimensional coefficients:

$$C_L = \frac{F_z}{\frac{1}{2}\rho U_\infty^2 \mathcal{A}}, \quad C_D = \frac{F_x}{\frac{1}{2}\rho U_\infty^2 \mathcal{A}}, \quad C_M = \frac{M_y}{\frac{s}{2} F_{\text{ref}}}, \tag{14}$$

where the forces and moments are decomposed in the frame shown in Fig. 12, with x parallel to the freestream velocity, $y = Y$ pointing to the starboard of the aircraft, and z upwards. Also, $\mathcal{A} = 4\pi R^2$ is the total rotor area, F_{ref} is the thrust produced by a single rotor when the drone is hovering, and $s/2$ is the lever arm between the center of the airframe and the rotor shaft. The pitching moment is computed about the center of the airframe, which we consider to be the center of gravity of the system.

As a result of the different revolution frequency of the front and rear rotors, beating is observed in the instantaneous time signals, with a characteristic period of $T_b = 1/(\text{bpf}_{\text{rear}} - \text{bpf}_{\text{front}})$. For 2-bladed rotors, the blade passage frequency is twice the revolution frequency, bpf $= 2n$. It follow that $T_b = 0.04$ s. Figure 13 spans $2T_b$ so that the beating of instantaneous quantities can be observed. The averaged total forces and moment, on the other hand, result from the application of a sliding mean operator, with a window size equal to T_b.

The time-averaged total lift force computed (12.46 N) is well in the range of the nominal weight of Phantom drones (11.77 to 13.73 N) which have a mass between 1.2 and 1.4 kg. As further required for trim, the net average streamwise force is close to zero since the thrust of the rotors balances the drag of the airframe. The net average pitching moment is also zero. The contribution from the airframe results in a slight pitch-up moment that is balanced by the

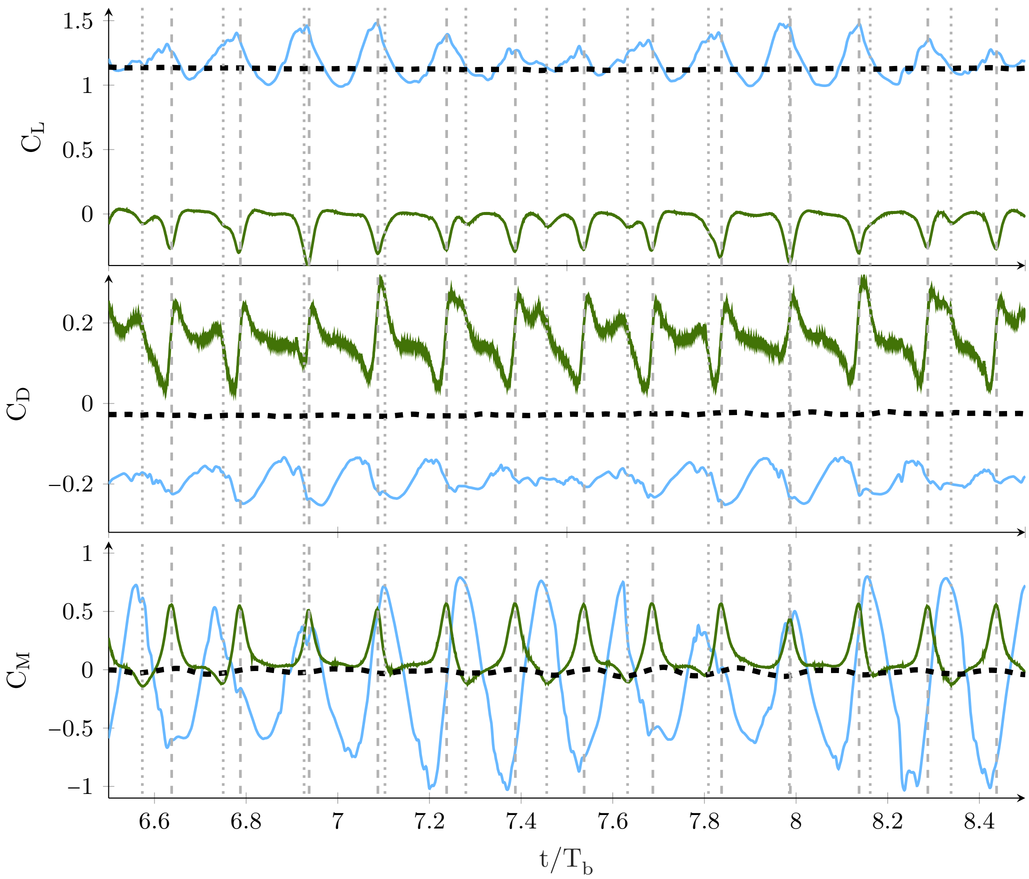

Figure 13: Lift (top), drag (middle), and pitching moment (bottom) measured in the *"with airframe"* case. Contributions from the airframe (—), from the rotors (—), and time-average of their sum (▪ ▪). Faded vertical lines identify the times when a blade passes right above the airframe leg on the front (····) and rear (- -) rotors.

pitch-down contribution of the rotors. The sum of the airfoil zero-lift moment from all blades is found to be negligible. Note that, if all rotors were rotating at the same speed, the net contribution from the rotor would be a pitch-up moment. This is mainly due to the edgewise force developed by rotors under a skewed inflow (as will be seen hereafter): when multiplied by the lever arm h_b, it results in a pitch-up moment. In trimmed forward flight, the rear rotors must thus rotate faster to balance the moment generated by both the airframe and the rotor edgewise forces.

As a verification of the reliability of our results, we note that our trimmed control inputs are similar to those computed by Thai et al. [47]. They proposed a trimming algorithm that uses the results of unsteady RANS simulations, and applied it to a DJI drone at various forward flight speeds. Only a high-level comparison with their trim solution is possible here, since our generic DJI slightly differs from their model of the Phantom 3. For $U_\infty = 10$, the ratio between their front and rear rotor n (approximately 1.25) is close to ours (1.18), and both our and their solutions use $\theta_v = -13°$. However, our rotational speeds are higher by 10% to 15%. This can be explained by two factors: 1) the drone is arbitrarily lighter in their study (about 1.0 kg); 2) the design of the propeller blades is different in each study, which leads to different thrust versus rotor speed characteristics.

5.2. Rotor-airframe aerodynamic interactions

5.2.1. On the airframe

The instantaneous forces and moment of the airframe shown in Fig. 13 clearly feature peaks occurring periodically. Those peaks are a direct consequence of the interactional aerodynamics between the rotors and the airframe, with frequencies corresponding to the blade passage frequency of the front and rear rotors.

Distinctly visible on the top plot, the lift force of the airframe drops every time a blade passes above a leg of the airframe. This can be understood as the effect of the local high pressure associated with the pressure side of each blade when it comes in proximity with the airframe. In fact, Wang et al. [48] measured these pressure peaks in a hover experiment they performed on a similar geometry. In the present simulation, the size of the peak induced by rear rotor blades is larger than that induced by front rotor blades, for a reason that will become clear in the next subsection.

The effect on the drag is less obvious but works the same way. For front rotors, the drag decreases right before the blade passes above a leg, and increases right after. The opposite is true for the rear rotors. This is due to the X-shape of the airframe. The high pressure below the blade induces a non-zero axial force when the blade is in the vicinity of the leg, oriented forward when the blade is slightly behind, and backward when slightly in front.

Finally, the pitching moment of the airframe experiences a sudden increase (respectively decrease) when a blade from the front (resp. rear) rotor passes right above the airframe leg. This is consistent with what we observe on the lift and considering the lever arm between each rotor and the drone center.

5.2.2. On the rotors

To understand how each blade operates over the course of a revolution, we present polar plots of the angle of attack α in Fig. 14a and of the sectional normal force f_Z in Fig. 14b. f_Z is the projection of the blade sectional force (lift and drag) on the Z direction. The quantities shown in the figure are phase averaged over the last ten revolutions of each rotor.

The angle of attack provides information about the local flow direction. For example, the signature mild BVIs is visible on all four rotors, materialized by sharp gradients. Comparing the angle of attack with and without the airframe helps describe the potential interaction with the airframe. In fact, the airframe must induce local updrafts and downdrafts due to the blockage. If the flow was potential, we would expect to observe an increase in α in front of each airframe leg, and a decrease behind.

What we observe instead on the front rotor in Fig. 14a is an increase in α everywhere in the vicinity of the leg. We attribute the locally high angles of attack to an interaction with the preceding tip vortex which has to flow around the airframe. Because of the blockage by the airframe, the tip vortex remains close to the blade when it passes above the leg, inducing a higher angle of attack. On the other hand, the rear rotors exhibit a slight reduction in angle of attack right behind the leg, which is consistent with our initial expectation.

It must be noted that the time when the blade and the airframe are the closest occurs on the retreating side for the front rotors and on the advancing

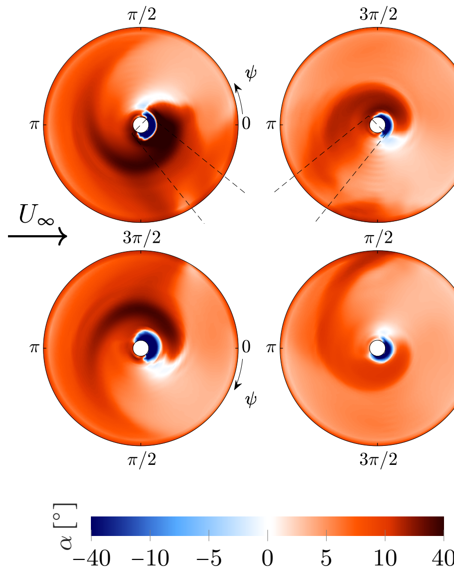

(a) Angle of attack

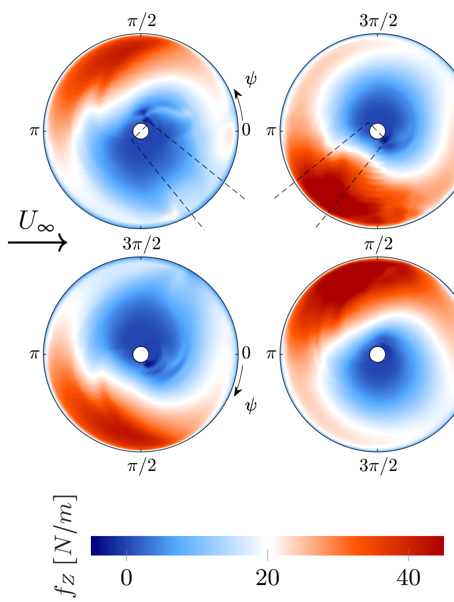

(b) Sectional lift

Figure 14: Polar representation of blade aerodynamic quantities phase-averaged over 10 rotor revolutions. Top rows show rotors 2 and 3 of the *"with airframe"* case, bottom rows show rotors 1 and 4 of the *"no airframe"* case. ψ is the azimuthal angle, positive in the direction of spin. Dashed lines show the projection of the airframe on the rotor planes.

side for the rear rotors. Due to the smaller relative velocity, the normal force is always smaller on the retreating side, as can be seen in Fig. 14b. In fact, most of the lift of each rotor is produced in the fore part on the advancing side. Therefore, the consequence of the rotor-airframe interaction is more pronounced for the rear rotors, as high blade loading coincides with airframe proximity. This explains why the peak airframe loads associated with the rear rotors in Fig. 13 are larger.

To elaborate on the effect of the interactions on the rotors, we compare the instantaneous rotor loads in the cases with and without airframe. In the latter simulation, the trim inputs $(n_{\mathrm{front}}, n_{\mathrm{rear}}, \theta_v)$ are kept the same as in the *"with airframe"* case so that the effect of the airframe can be isolated. Figure 15 presents the forces and the pitching moment resulting from the contribution of all rotors. The comparison reveals that the presence of the airframe only slightly affects the rotor loads. Despite the local changes in angle of attack reported previously, the sum of the forces generated by all rotors are little affected by the presence of the airframe.

To further assess the influence of the airframe on each rotor individually, Fig. 16 presents the rotor force and moment coefficients computed in the cases with and without airframe. Here, the forces F and moments M are calculated in the drone frame (shown in Fig. 9). The moments are calculated about their respective rotor center.

We choose to compare the values for rotor 2 and 4 (front right and rear left) since they are spinning in the same direction. In light of the load assessment presented in Section 3.1, the values reported in the figure should not be interpreted as definite. However, their relative comparison allows us to highlight the effect of the various aerodynamic interactions. Note that, considering the quadcopter pitch angle θ_v, the rotors are oriented in the flow with an angle $\gamma = 77°$ based on the definition shown in Fig. 5. At this angle, we did not observe the blades cutting through the tip vortices, as was the case at $\gamma = 90°$ in Section 3.1. Therefore, the predicted loads should not suffer as much from an inaccurate modeling of strong BVI.

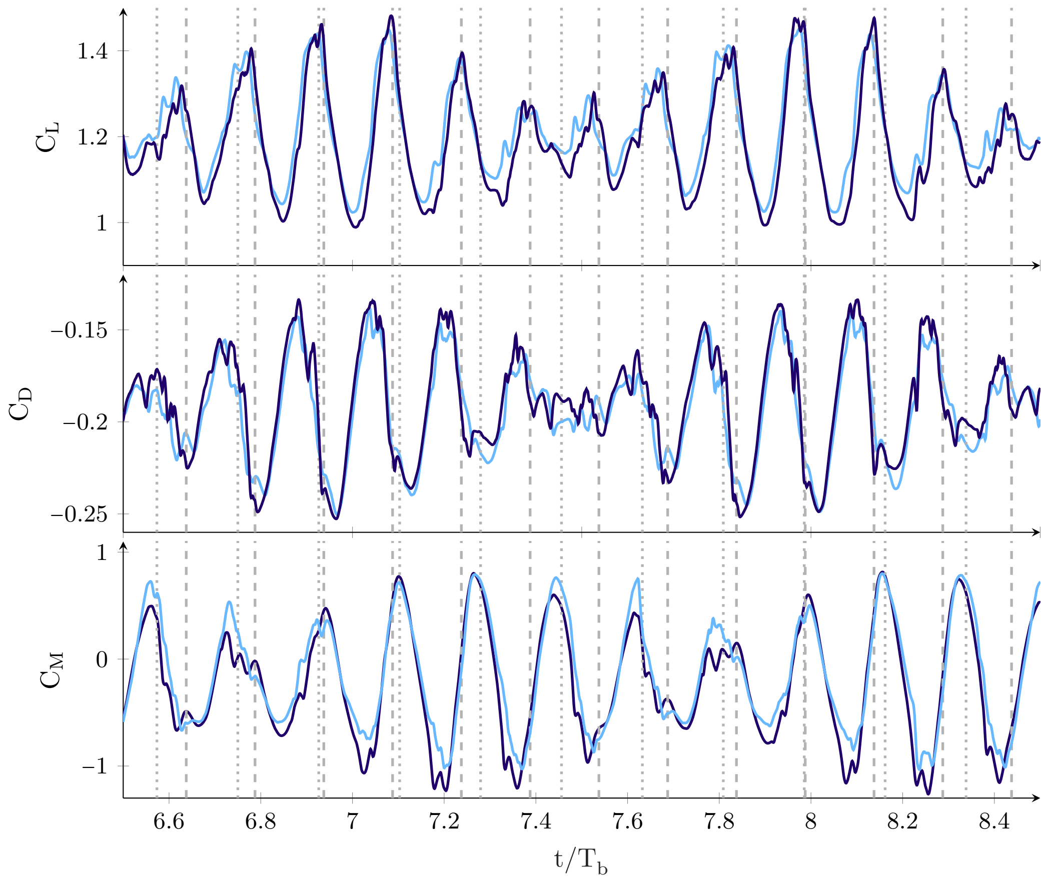

Figure 15: Lift (top), drag (middle), and pitching moment (bottom) from the rotors evaluated in the *"no airframe"* case (—) and in the *"with airframe"* case (—).

Looking at the force coefficients first (the top row in the plot), the effect of the rotor-rotor interaction is visible in both cases. Rotor 4 has a 6 to 8 % smaller average thrust coefficient than rotor 2. The same trend had been identified in previous studies ([3], among others). A similar observation can be made on C_X, while C_Y remains mostly close to zero. Note the positive C_X of all rotors, which contribute to the total aircraft pitching moment, as explained earlier. The presence of the airframe slightly affects the average force coefficients, towards a small reduction of the thrust coefficient of the rear rotor (about 2.4%). These results confirm the relative insensitivity of the rotor forces to the presence of the

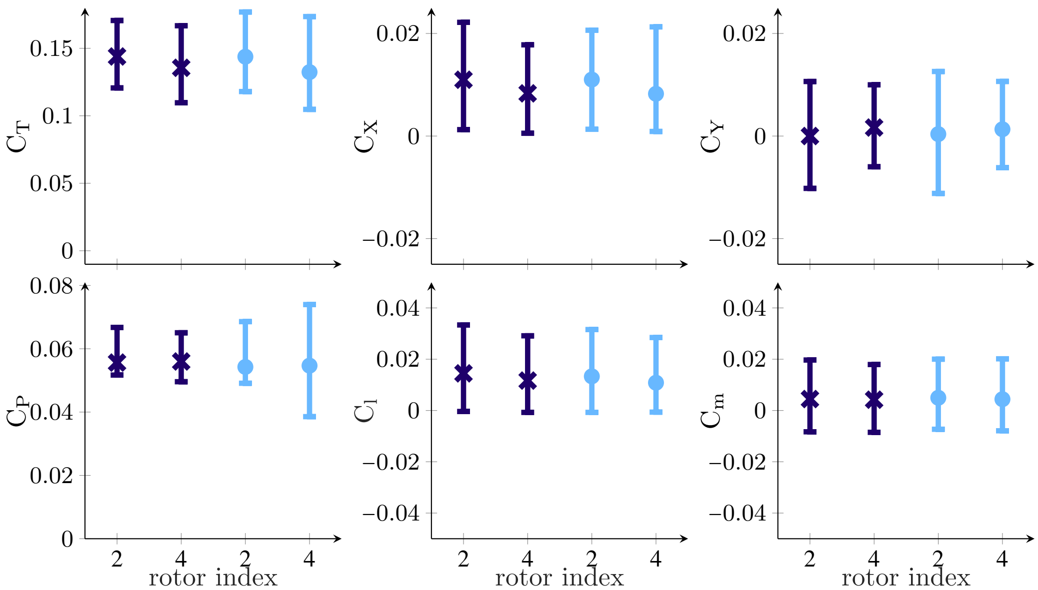

Figure 16: Rotor coefficients evaluated in the *"no airframe"* case ( ) and in the *"with airframe"* case ( ). The bars show the range between min and max values, and the symbol represent the value averaged over $3T_b$.

airframe, which we already reported previously based on the total aircraft aerodynamic coefficients. However, we note that the *"with airframe"* case generally exhibits larger amplitude fluctuations in the thrust and the edgewise forces.

The average rotor power (or equivalently the rotor torque) coefficient varies by less than 2% across all cases and all rotors. However, the amplitude of the fluctuations is clearly increased by the presence of the airframe, especially for the rear rotor. The average rolling moment shows trends similar to C_X, while the pitching moment is mostly constant across all cases. The amplitude of the corresponding fluctuations seems unaffected by the airframe.

5.2.3. Summary

We provide a numerical summary of the average lift, drag and pitching moment coefficients of the aircraft in Table 3. The rotor contributions to the aircraft lift and drag coefficients change by less than 2% between the cases with and without airframe. Consequently, a good approximation of the sum of the

Table 3: Summary of the average aircraft aerodynamic coefficients. Relative differences are computed using the *"no airframe"* case as a reference.

		"no airframe"	*"with airframe"*	*relative* Δ
$\mathbf{C_L}$	*total*	1.210	1.124	−7.13%
	rotors	1.210	1.191	−1.61%
	airframe	—	−0.067	—
$\mathbf{C_D}$	*total*	−0.194	−0.023	+87.9%
	rotors	−0.194	−0.190	+1.93%
	airframe	—	0.167	—
$\mathbf{C_M}$	*total*	−0.225	−0.018	+92.2%
	rotors	−0.225	−0.139	+38.1%
	airframe	—	0.121	—

forces produced by the rotors can be obtained when the airframe is neglected. This gives credit to common modeling techniques that neglect the aerodynamic interactions with the airframe when evaluating the average rotor loads. The instantaneous rotor loads are in fact only slightly affected by the presence of the airframe, the primary effect being a local modification of the angle of attack of the blades because of the blockage associated with the airframe legs. Nevertheless, the rotor contribution to the average aircraft pitching moment is sensitive to the presence of the airframe. This is mostly because the thrust coefficient of the rear rotors is lower when the airframe is present (which also explains the change in the C_L contribution). The average of the other rotor force and moment coefficients are mostly unaffected by the presence of the airframe. The amplitude of their fluctuations is however increased, especially for the thrust and torque coefficients.

Our calculations also confirm that rotor-rotor aerodynamic interactions substantially affect the rear rotor performance, and hence the trim conditions of the entire aircraft. The present simulations inherently capture those interactions, and their effects were included in the trim parameters reported in Table 2.

As far as the airframe is concerned, the forces and moments are strongly dependent on the local flow conditions that include the rotor washes. If the rotor is close enough to the airframe, the local high pressure in the vicinity of the blade pressure side also adds a peak to the airframe loads.

5.3. Wake results

In this section, we analyze the wakes resulting from our simulations of the cases with and without airframe. In both cases, the vorticity in the wake is fully unsteady and originates from the shedding occurring on the rotors and on the airframe. The study of unsteady wakes often relies on the analysis of time-averaged quantities. Their computation first requires an appropriate definition of averaging, especially in the present case of a quadcopter with different rotor speeds.

The characteristic shedding frequency of the rotors corresponds to their blade passage frequencis, $\mathrm{bpf}_{\mathrm{rear}}, \mathrm{bpf}_{\mathrm{front}}$ [22]. Since the front and rear rotors rotate at different speeds, we must determine the period that corresponds to the entire rotor system returning to the same absolute state, that is, the actual periodicity of the system. This period is $T_w = \mathrm{lcm}(1/\mathrm{bpf}_{\mathrm{rear}}, 1/\mathrm{bpf}_{\mathrm{front}})$, where lcm denotes the least common multiple. In the near wake region at least, T_w should thus be the actual period over which any instantaneous wake quantity is periodic. Note, however, that the shedding of vorticity from the airframe may introduce perturbations that are aperiodic.

For the present wake analysis, statistics are obtained by averaging instantaneous wake quantities over T_w. Incidentally, for the rotor speeds reported in Table 2, $T_w = 0.12\ s$ also corresponds to $3T_b$. This partially motivated the choice of the RPM values in the first place, to avoid an arbitrary large T_w. Also, having kept the same rotational speed for the rotors in the simulations of the cases with and without airframe facilitates the comparison of their wakes.

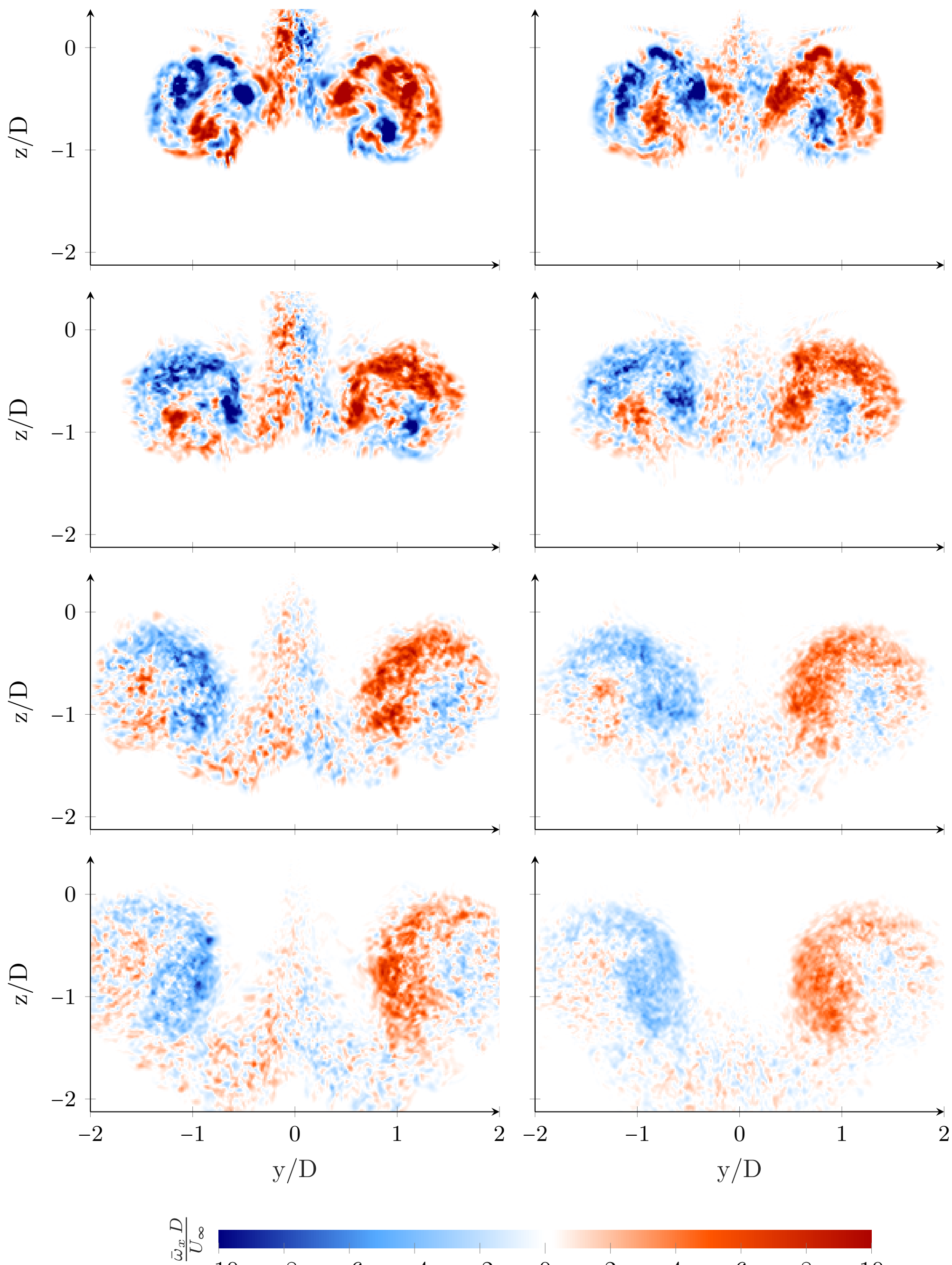

Figure 17: Time-averaged axial vorticity $\bar{\omega}_x$ in slices located at $x/D = 2, 3, 5, 7$ (from top to bottom) in the wake of the *"no airframe"* case (left) and of the *"with airframe"* case (right).

5.3.1. Flow field

We evaluate the vorticity in slices of the flow normal to the upstream velocity. Figure 17 shows the average streamwise vorticity at different downstream locations. Distances are measured from the center of the drone. In the first two slices, distinct patches of vorticity of alternate signs are visible. They attest to the coherence of the average vorticity shed by the rotating blades. Farther downstream, a single patch starts to dominate on each side under the action of turbulent mixing and vortex interactions. Eventually, vorticity of a single sign mostly remains on each side, which corresponds to the establishment of the main wake vortices. Note that, even in the downstream-most slice, the roll-up of these wake vortices is not yet completed as they are not axisymmetric.

Comparing the average axial vorticity in the wake of the two cases, we note that the airframe has two tangible effects. First, it affects the spatial extent of the wake, which tends to be slightly more compact in the *"with airframe"* case. Second, it influences the development of the vorticity in the wake mid plane ($y = 0$). In the *"no airframe"* case, a soaring flow feature is visible in the mid plane. This had been already observed by Wang et al. [15]. It is formed by a vorticity dipole that advects upwards. The dipole originates in the interaction of the trailing vorticity generated at the inboard edge of all four rotors. When the airframe is present in the simulation, it alters the vorticity generation mechanism and it enhances the turbulence mixing. Consequently, the soaring feature disappears almost completely.

We should emphasize that, for the current quadcopter configuration, it is critical to distinguish between instantaneous and time-averaged vorticity in the wake. The time-averaged vorticity allows us to make conclusions regarding the coherence of the average flow. However, this coherence may not be apparent when the instantaneous vorticity is considered. For example, Fig. 18 shows the instantaneous vorticity field evaluated at $x/D = 5$. It is very different from Fig. 17: no large-scale coherent vortex can be observed at any given time. Instead, it shows the complexity of the flow and the large number of small scale

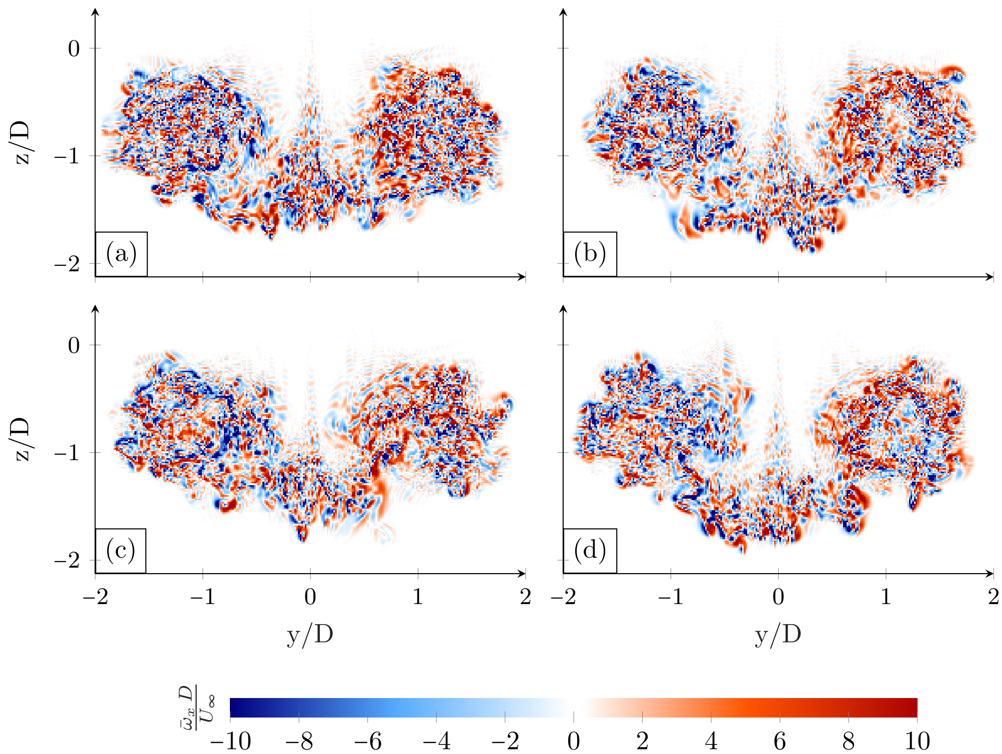

Figure 18: Instantaneous axial vorticity ω_x in a slice located at $x/D = 5$ behind the *"with airframe"* case, evaluated at four times uniformly spaced over T_w from (a) to (d).

vortices that result from rotor-shed vortices interacting with each other, and with the wake of the airframe. This is a departure from the wakes of airplane wings or helicopter rotors where a coherent vortex core is generally visible even in the instantaneous vorticity field. In the present case of the quadcopter, the large mixing occurring in the near wake results in a highly unsteady, turbulent flow. The mixing also contributes to the spatial spreading of the vorticity, which explains why the average wake vortices do not clearly feature a well-defined vortex core. We further discuss the wake generation process in [17] and compare the wakes shed by various UAM vehicles. Although not discussed here, the instantaneous velocity field in the wake slice is provided in the supplemental data repository [38] for the interested reader.

5.3.2. Wake properties

A quantitative description of the wake can be performed using standard metrics. We first recall some wake properties that are conventionally used for wake characterization. They can all be obtained from 2D slices of the wake. The vertical impulse in a slice is defined as

$$I_w = \Gamma_w b_w = \int_{-\infty}^{\infty} \int_{-\infty}^{\infty} y\, \bar{\omega}_x \, dy \, dz. \tag{15}$$

Since the vorticity is compactly supported inside the computational domain, we replace the integral bounds by the domain boundaries. For the wake vortex circulation, we use the definition proposed in [17] that suits well the case of a quadcopter wake,

$$\Gamma_w = \max_y \int_{-\infty}^{\infty} \int_{y}^{\infty} \bar{\omega}_x \, dy \, dz. \tag{16}$$

Finally, the vortex spacing is a measure of the distance between the port and starboard vortex. It is defined as

$$b_w = \frac{I_w}{\Gamma_w}. \tag{17}$$

We calculate the circulation and spacing in our simulations of both cases. Results are reported in Fig. 19. The circulations are initially different, but then converge to very similar values after $4D$ behind the aircraft. In fact, the relative difference between the circulations computed at $x/D = 5$ and 7 is smaller than 0.2%. This means that the presence of the airframe does not affect the strength of the wake vortices in the far field. However, the presence of the airframe alters the spacing of the vortices, as already postulated in the previous section. The measure of b_w indeed shows a smaller value in the wake of the *"with airframe"* case, hence a more compact wake. Note that we normalized the vortex spacing with respect to the aircraft span b, as classically done in wake studies. For the generic DJI geometry, we have $b = D + s = 0.49\ m$.

Finally, we demonstrate the high level of fluctuation in the wake using a measure of the resolved turbulent kinetic energy,

$$\bar{k} = \frac{1}{2}\left(\overline{u'u'} + \overline{v'v'} + \overline{w'w'}\right), \tag{18}$$

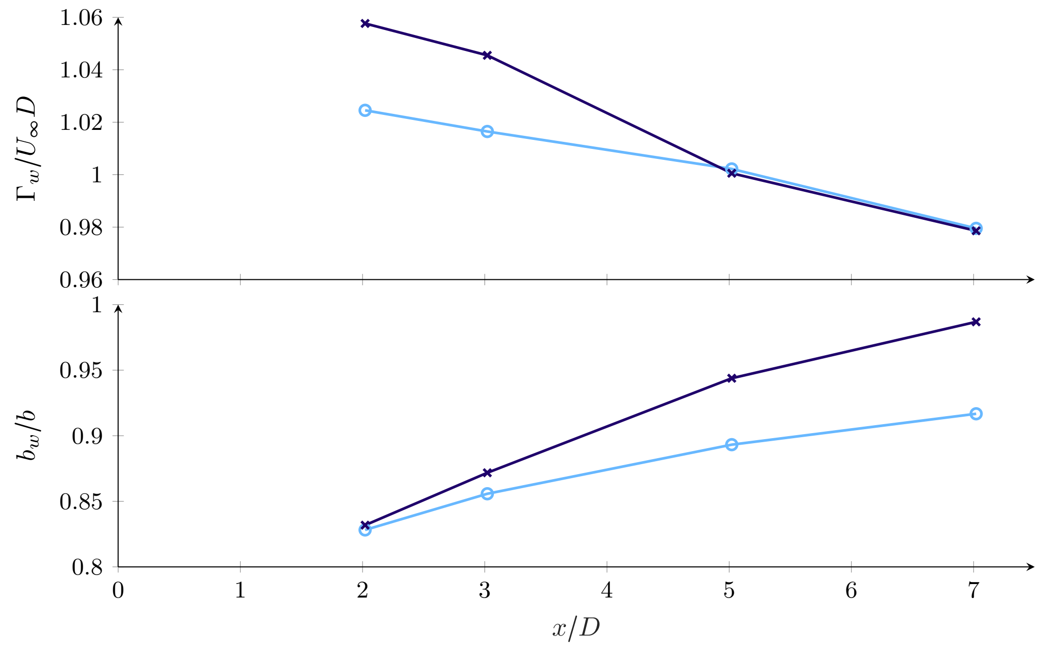

Figure 19: Wake vortex circulation (top) and spacing (bottom) calculated in the wake of the *"no airframe"* case ( ) and of the *"with airframe"* case ( ).

where u', v', w' are the velocity fluctuations with $u' = u - \bar{u}$, etc. The total energy related to these oscillations in a slice can be obtained as

$$E' = \int_{-\infty}^{\infty} \int_{-\infty}^{\infty} \bar{k} \, dy \, dz. \tag{19}$$

Figure 20 shows E' calculated at the same four slices in the wake. We can see that the presence of the airframe is associated with an increase in the level of fluctuation in the very near wake, but those fluctuations then dampens slightly faster than in the wake of the *"no airframe"* case. Finally, we note that E' is almost one order of magnitude higher than the values reported in the wake of a conventional helicopter in forward flight [22]. This reinforces our claim that the interactions between the vortices emanating from the four rotors of the quadcopter lead to a significantly higher turbulent mixing.

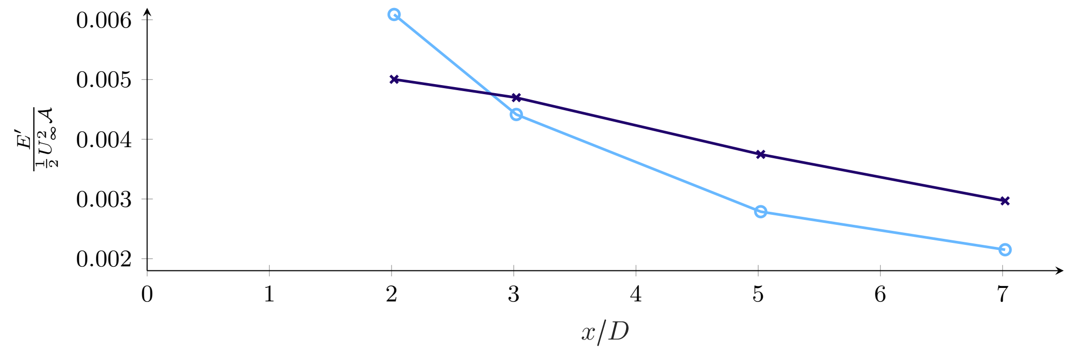

Figure 20: Energy of the velocity fluctuations calculated in the wake of the *"no airframe"* case ( ) and of the *"with airframe"* case ( ).

6. Conclusions

In this work we investigated the effect of the rotor-airframe interaction on the aeromechanics of a quadcopter in forward flight, and on the development of its wake. This effect was highlighted by comparing the results of large-eddy simulation using a Vortex Particle–Mesh method. In the simulations, the rotor blades were modeled through immersed lifting lines. The numerical method was here augmented with a penalization technique to model the presence of the airframe in the flow. The performance of the models was assessed by comparing their predictions with experimental data for two representative configurations, and demonstrated that the models worked as intended.

We defined and studied a generic drone geometry that represents simply the shape of a realistic drone. To isolate the effect of the rotor-airframe interaction, we simulated and compared two configurations: one including the rotors and the drone airframe, and the other considering only the rotors. After the verification of the trim conditions, we evaluated the forces and moments on each part of the drone and we computed appropriate time-averages. We showed that the rotor-airframe interaction leads to peaks in the loads experienced by the airframe. They were attributed to the effect of the high pressure in the vicinity of the blade pressure side. On the other hand, the total force generated by all rotors differed by less than 2% between the simulation with and without the airframe, even though the flow conditions are locally altered by the blockage associated with the airframe. The time-averaged forces and moments of each rotor individually further proved relatively insensitive to the presence of the airframe, with the thrust coefficient of the rear rotor varying by maximum 2.4%. However, we observed an increase in the fluctuation of the thrust and power coefficients when the airframe is included. Hence, for geometries similar to that studied here, a general conclusion regarding modeling of the rotor forces is that the rotor-airframe interaction can be neglected when computing the average loads of the rotors. However, it must be accounted for to accurately represent the loads on the airframe, and the total pitching moment of the quadcopter (both rotor and airframe contributions). Rotor-rotor interactions should also not be overlooked as we could observe them significantly affecting the rear rotor performances.

In addition to forces and moments, we studied the effect of the airframe on the development of the quadcopter near wake. Our results first showed the inherently unsteady (i.e., turbulent) character of the vorticity in the wake of the drone, which exhibits coherence only in a time-averages sense. Comparing the wake of the drone with and without airframe, we determined that their circulation converges to similar values (less than 0.2% different) at increasing downstream distances, which indicates that the airframe does not affect the far-field wake strength. However, the lateral extent of the wake is smaller in the simulation with the airframe, as demonstrated both by the visual examination of the vorticity in the wake, and by the calculation of the wake vortex spacing.

Even though this study focused on a relatively small-scale drone, our conclusions regarding the effect of the rotor-airframe interaction should still hold for larger UAM vehicles. In particular, the blockage fraction —i.e., considering the projection of the airframe on the four rotor disks, the ratio between the area occupied by the airframe and the total rotor area— is relatively high for our generic drone. The higher this fraction, the more prominent we expect the rotor-airframe interactions to be. As typical UAM vehicles are associated with smaller ratios, the effect of the rotor-airframe interaction should be similar but less pronounced than those evaluated in the present study.

Data availability

Supplemental data repository [38]: *Large eddy simulation of a quadcopter in forward flight: aeroloads and wake*, `https://doi.org/10.5281/zenodo.6506834`.

This repository contains the following underlying data:

- the numerical values used in the figures of this paper;
- the time-resolved signal of the blade and airframe forces and moment for each quadcopter simulation;
- a subset of the full time-resolved velocity field gathered in one cross section of each quadcopter wake (with and without the body).

Data are available under the terms of the Creative Commons Attribution-ShareAlike 4.0 International Public License (CC-BY-SA 4.0). Additional information can be obtained from the authors upon reasonable request.

Acknowledgments

The authors are grateful for the computing resources provided by the Office of Research Computing at Brigham Young University. D.-G. Caprace acknowledges the financial support received from a Wallonie-Bruxelles International (WBI) excellence fellowship.

References

[1] W. Johnson, C. Silva, Observations from exploration of vtol urban air mobility designs, in: The Asian/Australian Rotorcraft Forum, Jeju Island, Korea, 2018.

[2] Y. Yang, Y. Liu, Y. Li, E. Arcondoulis, Y. Wang, Aerodynamic and aeroacoustic performance of an isolated multicopter rotor during forward flight, AIAA Journal 58 (2020) 1171–1181. doi:`10.2514/1.J058459`.

[3] T. C. A. Stokkermans, D. Usai, T. Sinnige, L. L. M. Veldhuis, Aerodynamic interaction effects between propellers in typical evtol vehicle configurations, Journal of Aircraft 58 (2021) 1–19. doi:10.2514/1.C035814.

[4] T. C. A. Stokkermans, L. L. M. Veldhuis, Propeller performance at large angle of attack applicable to compound helicopters, AIAA Journal 59 (2021) 2183–2199. doi:10.2514/1.J059509.

[5] J. Y. Hwang, M. K. Jung, O. J. Kwon, Numerical study of aerodynamic performance of a multirotor unmanned-aerial-vehicle configuration, Journal of Aircraft 52 (2015) 839–846. doi:10.2514/1.C032828.

[6] M. Misiorowski, F. Gandhi, A. A. Oberai, Computational study on rotor interactional effects for a quadcopter in edgewise flight, AIAA Journal 57 (2019) 5309–5319. doi:10.2514/1.J058369.

[7] O. Pinti, A. A. Oberai, R. Healy, R. J. Niemiec, F. Gandhi, Multi-fidelity approach to predicting multi-rotor aerodynamic interactions, AIAA Journal (2022) 1–15. doi:10.2514/1.J060227.

[8] P. Ventura Diaz, S. Yoon, High-fidelity computational aerodynamics of multi-rotor unmanned aerial vehicles, in: 2018 AIAA SciTech Forum, 2018. URL: https://arc.aiaa.org/doi/abs/10.2514/6.2018-1266. doi:10.2514/6.2018-1266.

[9] P. Ventura-Diaz, S. Yoon, High-fidelity simulations of a quadrotor vehicle for urban air mobility, in: AIAA SCITECH 2022 Forum, 2022. URL: https://arc.aiaa.org/doi/abs/10.2514/6.2022-0152. doi:10.2514/6.2022-0152.

[10] N. van Arnhem, R. de Vries, T. Sinnige, R. Vos, G. Eitelberg, L. L. M. Veldhuis, Engineering method to estimate the blade loading of propellers in nonuniform flow, AIAA Journal 58 (2020) 5332–5346. doi:10.2514/1.J059485.

[11] J. Luo, L. Zhu, G. Yan, Novel quadrotor forward-flight model based on wake interference, AIAA Journal 53 (2015) 3522–3533. doi:10.2514/1.J053011.

[12] D. Barcelos, A. Kolaei, G. Bramesfeld, Aerodynamic interactions of quadrotor configurations, Journal of Aircraft 57 (2020) 1074–1090. doi:10.2514/1.C035614.

[13] C. H. J. Wang, J. C. Nathanael, E. M. Ng, B. F. Ng, K. H. Low, Framework for the estimation of safe wake separation distance between same-track multi-rotor uas, in: AIAA Scitech 2021 Forum, 2021. URL: https://arc.aiaa.org/doi/abs/10.2514/6.2021-0708. doi:10.2514/6.2021-0708.

[14] C. J. Wang, K. H. Low, Software-in-the-loop investigation of wake-vortex-encounter-response of identical multirotor pair with px4 attitude controller, Aerospace Science and Technology 117 (2021) 106967. doi:https://doi.org/10.1016/j.ast.2021.106967.

[15] C. H. J. Wang, J. C. Nathanael, K. H. Low, Numerical investigation on influence of fuselage on multirotor wake vortex structures in forward flight, in: AIAA SCITECH 2022 Forum, 2022. URL: https://arc.aiaa.org/doi/abs/10.2514/6.2022-0151. doi:10.2514/6.2022-0151.

[16] J. C. Nathanael, C.-H. J. Wang, K. H. Low, Numerical studies on modeling the near- and far-field wake vortex of a quadrotor in forward flight, Proceedings of the Institution of Mechanical Engineers, Part G: Journal of Aerospace Engineering 236 (2022) 1166–1183. doi:10.1177/09544100211029074.

[17] D.-G. Caprace, A. Ning, Large eddy simulation of the wakes of three urban air mobility vehicles, in: Vertical Flight Society 78th annual forum, 78-2022-0063, Fort Worth, Texas, 2022.

[18] E. J. Alvarez, A. Ning, High-fidelity modeling of multirotor aerodynamic interactions for aircraft design, AIAA Journal 58 (2020) 4385–4400. doi:10.2514/1.J059178.

[19] A. Zanotti, A. Savino, M. Palazzi, M. Tugnoli, V. Muscarello, Assessment of a mid-fidelity numerical approach for the investigation of tiltrotor aerodynamics, Applied Sciences 11 (2021). doi:10.3390/app11083385.

[20] P. Chatelain, M. Duponcheel, S. Zeoli, S. Buffin, D.-G. Caprace, G. Winckelmans, L. Bricteux, Investigation of the effect of inflow turbulence on vertical axis wind turbine wakes, Journal of Physics: Conference Series 854 (2017) 012011. doi:10.1088/1742-6596/854/1/012011.

[21] P. Chatelain, M. Duponcheel, D.-G. Caprace, Y. Marichal, G. Winckelmans, Vortex particle-mesh simulations of vertical axis wind turbine flows: from the airfoil performance to the very far wake, Wind Energy Science 2 (2017) 317. doi:10.5194/wes-2-317-2017.

[22] D.-G. Caprace, P. Chatelain, G. Winckelmans, Wakes of rotorcraft in advancing flight: A large eddy simulation study, Physics of Fluids 32 (2020) 087107. doi:10.1063/5.0015162.

[23] D.-G. Caprace, G. Winckelmans, P. Chatelain, Assessment of the vortex particle-mesh method for efficient LES of hovering rotors and their wakes, in: AIAA Scitech 2021 Forum, 2021. doi:10.2514/6.2021-0738.

[24] P. Chatelain, P. Koumoutsakos, A Fourier-based elliptic solver for vortical flows with periodic and unbounded directions, Journal of Computational Physics 229 (2010) 2425–2431. doi:10.1016/j.jcp.2009.12.035.

[25] G. S. Winckelmans, Encyclopedia of Computational Mechanics, John Wiley & Sons, Ltd, 2004, pp. 129–153. doi:10.1002/0470091355.ecm055.

[26] C. Mimeau, I. Mortazavi, A review of vortex methods and their applications: From creation to recent advances, Fluids 6 (2021). doi:10.3390/fluids6020068.

[27] P. Chatelain, A. Curioni, M. Bergdorf, D. Rossinelli, W. Andreoni, P. Koumoutsakos, Billion vortex particle Direct Numerical Simulations of

aircraft wakes, Computer Methods in Applied Mechanics and Engineering 197 (2008) 1296–1304. doi:10.1016/j.cma.2007.11.016.

[28] I. F. Sbalzarini, J. H. Walther, M. Bergdorf, S. E. Hieber, E. M. Kotsalis, P. Koumoutsakos, PPM A highly efficient parallel particle mesh library for the simulation of continuum systems, J. Comput. Phys. 215 (2006) 566–588. doi:10.1016/j.jcp.2005.11.017.

[29] D.-G. Caprace, G. Winckelmans, P. Chatelain, An immersed lifting and dragging line model for the vortex particle-mesh method, Theoretical and Computational Fluid Dynamics 34 (2020) 21–48. doi:10.1007/s00162-019-00510-1.

[30] P. Angot, C. Bruneau, P. Fabrie, A penalization method to take into account obstacles in incompressible viscous flows, Numerische Mathematik 81 (1999) 497–520.

[31] W. M. van Rees, M. Gazzola, P. Koumoutsakos, Optimal shapes for anguilliform swimmers at intermediate reynolds numbers, Journal of Fluid Mechanics 722 (2013) R3. doi:10.1017/jfm.2013.157.

[32] G. Carbou, P. Fabrie, Boundary layer for a penalization method for viscous incompressible flow, Adv. Differential Equations 8 (2003) 1453–1480.

[33] J. T. Rasmussen, G.-H. Cottet, J. H. Walther, A multiresolution remeshed Vortex-In-Cell algorithm using patches, Journal of Computational Physics 230 (2011) 6742–6755. doi:10.1016/j.jcp.2011.05.006.

[34] C. Mimeau, G.-H. Cottet, I. Mortazavi, Direct numerical simulations of three-dimensional flows past obstacles with a vortex penalization method, Computers & Fluids 136 (2016) 331 – 347. doi:10.1016/j.compfluid.2016.06.020.

[35] M. Hejlesen, J. Rasmussen, A. Larsen, J. H. Walther, On estimating the aerodynamic admittance of bridge sections by a mesh-free vortex method,

Journal of Wind Engineering and Industrial Aerodynamics 146 (2015) 117 – 127. doi:http://dx.doi.org/10.1016/j.jweia.2015.08.003.

[36] T. Gillis, G. Winckelmans, P. Chatelain, An efficient iterative penalization method using recycled Krylov subspaces and its application to impulsively started flows, Journal of Computational Physics 347 (2017) 490 – 505. doi:10.1016/j.jcp.2017.07.015.

[37] C. Bernier, M. Gazzola, R. Ronsse, P. Chatelain, Simulations of propelling and energy harvesting articulated bodies via vortex particle-mesh methods, Journal of Computational Physics 392 (2019) 34–55. doi:10.1016/j.jcp.2019.04.036.

[38] D.-G. Caprace, A. Ning, P. Chatelain, G. Winckelmans, DATASET: Large eddy simulation of a quadcopter in forward flight: aeroloads and wake, 2022. URL: https://doi.org/10.5281/zenodo.6506833. doi:10.5281/zenodo.6506833.

[39] M. Drela, Xfoil: An analysis and design system for low reynolds number airfoils, in: Low Reynolds number aerodynamics, Springer, 1989, pp. 1–12.

[40] L. A. Viterna, D. C. Janetzke, Theoretical and experimental power from large horizontal-axis wind turbines, Technical Report NASA-TM-82944, NASA, United States, 1982. URL: https://www.osti.gov/biblio/6763041. doi:10.2172/6763041.

[41] A. R. Meyer Forsting, G. R. Pirrung, N. Ramos-García, A vortex-based tip/smearing correction for the actuator line, Wind Energy Science 4 (2019). doi:10.5194/wes-2018-76.

[42] F. W. Roos, W. W. Willmarth, Some experimental results on sphere and disk drag, AIAA Journal 9 (1971) 285–291. doi:10.2514/3.6164.

[43] E. Berger, D. Scholz, M. Schumm, Coherent vortex structures in thewake of a sphere and a circular disk at rest and under forced vibrations, Journal of

Fluids and Structures 4 (1990) 231–257. doi:https://doi.org/10.1016/S0889-9746(05)80014-3.

[44] X. Tian, M. C. Ong, J. Yang, D. Myrhaug, Large-eddy simulations of flow normal to a circular disk at re=1.5×105, Computers & Fluids 140 (2016) 422–434. doi:https://doi.org/10.1016/j.compfluid.2016.10.023.

[45] Z. Ning, Experimental investigations on the aerodynamic and aeroacoustic characteristics of small UAS propellers, Ph.D. thesis, Iowa State University, Ames, 2018.

[46] W. Zhou, Z. Ning, H. Li, H. Hu, An experimental investigation on rotor-to-rotor interactions of small uav propellers, in: 35th AIAA Applied Aerodynamics Conference, 2017. URL: https://arc.aiaa.org/doi/abs/10.2514/6.2017-3744. doi:10.2514/6.2017-3744.

[47] A. Thai, B. Roget, J. Sitaraman, S. Grace, Multirotor trim using loose aerodynamic coupling, in: VFS Aeromechanics for Advanced Vertical Flight Technical Meeting, 2020.

[48] Z. Wang, Q. Henricks, M. Zhuang, A. Pandey, M. Sutkowy, B. Harter, M. McCrink, J. Gregory, Impact of rotor–airframe orientation on the aerodynamic and aeroacoustic characteristics of small unmanned aerial systems, Drones 3 (2019). doi:10.3390/drones3030056.